RSC Advances

PAPER

View Article Online
View Journal | View Issue

Cite this: *RSC Adv.*, 2026, **16**, 21561

Application of bimetallic gold–platinum nanoparticles in optical fiber sensors for pesticide detection

Nguyen Tran Truc Phuong, †[ab] Nguyen Do Quynh Nhu,†[cde] Le Hong Tho,[de] Do Thao Anh,[de] Quan-Doan Mai,[f] Vu Thi Huong,[g] Ting-Yu Liu,[hi] Khanh Q. Kieu,[j] Duc Anh Dinh[ab] and Nhu Hoa Thi Tran *[cd]

As chemical pesticides are widely applied to farming, rapid and ultrasensitive detection assays should be further designed for food safety and ecological health. Herein, we present a novel localized surface plasmon resonance (LSPR) optical fiber sensor using bimetallic Au@Pt core–shell nanoparticles for simultaneous detection of Quinalphos and Thiram. Four individual Au@Pt nanostructures (Au@Pt 1–4) were synthesized and a systematic change of the platinum precursor concentration was used to induce controlled evolution of the nanostructure from smooth shells to very dendritic assemblies. Detailed characterization *via* UV-Vis, FE-SEM, EDS, and HR-TEM revealed that the Au@Pt 3 sample, with a dendritic shell 12.5 nm thick, exhibited the optimal balance of specific surface area and plasmonic "hot spots". When integrated into a PDMS microfluidic channel, the Au@Pt 3-functionalized fiber sensor demonstrated high sensing performance. It could reach the ultralow detection limits (LOD) of 2.01×10^{-14} M for Quinalphos and LOD of 1.37×10^{-11} M for Thiram with a wide linear dynamic range. In addition, the sensor showed good reproducibility (RSD = 1.67%) and short-term stability (CV < 0.1%). These results also demonstrate the crucial influence of bimetallic morphology on LSPR activity and offer a promising platform for ultrasensitive pesticide detection.

Received 8th February 2026
Accepted 15th April 2026

DOI: 10.1039/d6ra01129b

rsc.li/rsc-advances

Introduction

The use of pesticides in modern agriculture has helped improve crop yields, but it also causes food safety and environmental and human health issues. Thiram is a fungicide that is used on fruits and vegetables, and its approval status in the European food-safety system is currently under review. This review is due to the fact that the European Union has set the maximum residue levels (MRLs) of Thiram to the detection limit value of 0.01 mg kg^{-1} with unresolved consumer safety concerns.[1] Quinalphos is an organophosphorus insecticide that continues to be used in some countries, and it causes neurotoxic effects and cholinesterase inhibition even at low doses.[2] Thiram and Quinalphos are trace residues that remain in agricultural products and groundwater; therefore, the process must be closely monitored. This is why we require pesticide residue testing in the environment and food that is fast, reliable, and highly sensitive.

Conventional analytical methods, including liquid chromatography (LC) and gas chromatography (GC) coupled with mass spectrometry (MS), represent the gold standard for pesticide residue detection. These techniques are recognized for their high separation efficiency and sensitivity.[3,4] While these multi-residue techniques can achieve low detection limits across a wide range of pesticides, they typically require complex equipment, sophisticated sample preparation, and specialized personnel, thereby restricting their use to centralized laboratory settings.[4] It is for this reason that optical fiber sensors are an emerging solution to these constraints. Thanks to their combination of fiber-optic platforms, remote sensing capabilities, compact size, immunity to electromagnetic interference, and optical transduction mechanisms, these sensors allow fast,

[a]*Center for Hi-Tech Development, Nguyen Tat Thanh University, Saigon Hi-Tech Park, Ho Chi Minh City, Vietnam*
[b]*NTT Hi-Tech Institute, Nguyen Tat Thanh University, Ho Chi Minh City, Vietnam*
[c]*Faculty of Materials Science and Technology, University of Science, Ho Chi Minh City, 700000, Vietnam. E-mail: ttnhoa@hcmus.edu.vn*
[d]*Viet Nam National University, Ho Chi Minh City, Vietnam*
[e]*Advanced Materials Technology Institute Viet Nam National University Ho Chi Minh City, Ho Chi Minh City, 700000, Vietnam*
[f]*Phenikaa University Nano Institute (PHENA), Phenikaa University, Hanoi, 12116, Vietnam*
[g]*Department of Chemistry, Soongsil University, Seoul, 06978, Republic of Korea*
[h]*Department of Materials Engineering, Ming Chi University of Technology, New Taipei City 243303, Taiwan*
[i]*Department of Chemical Engineering and Materials Science, Yuan Ze University, Taoyuan City 32003, Taiwan*
[j]*University of Arizona, Wyant College of Optical Sciences, 1630 E. University Blvd., Tucson, AZ 85719, USA*
† Nguyen Tran Truc Phuong and Nguyen Do Quynh Nhu contributed equally as co-first authors.

in-field, and potentially real-time monitoring.[5] Optical sensors based on evanescent-wave or plasmonic effects have been demonstrated to be effective in the detection of pesticides in environmental and food samples.[6] Sensors that are directly integrated into optical fibers offer greater flexibility, less sample volume, and the possibility of multiplexed detection. These attributes render optical fiber sensors highly suitable for monitoring residues of compounds such as Thiram and Quinalphos.

Among the various optical fiber sensing modalities, localized surface plasmon resonance (LSPR)-based sensors are recognized as highly sensitive and versatile tools for detecting chemicals and biomolecules. LSPR occurs when the collective oscillation of conduction electrons in metallic nanoparticles, driven by incident light at specific wavelengths, generates a highly confined electric field at the nanoparticle surface that extends only a short distance into the surrounding medium.[7] When these nanoparticles are immobilized on an optical fiber, at the tip, side, or within a tapered region, light propagating through the fiber interacts with the metal. Changes in the surrounding environment alter the local refractive index near the nanoparticles, inducing a measurable shift in the LSPR signal.[8,9]

The LSPR response is intrinsically linked to the morphology and composition of the nanostructures. While conventional spherical gold (Au) nanoparticles typically exhibit a single dipolar resonance mode, tailoring the shape and complexity – such as through the development of anisotropic or bimetallic nanostructures—enables the engineering of multiple hybridized modes and enhanced local field intensities.[10] As for fiber-based LSPR sensors, the enhancement of local field intensity due to the interaction of plasmonic nanoparticles with the guided optical mode tends to decrease the detection limit, which is usually in nanomolar or picomolar range of concentration of chemical analytes.[9] Compared to conventional surface plasmon resonance (SPR) sensors, which utilize continuous metallic films, LSPR systems offer reduced sensing volumes, sharper spectral features, and improved compatibility with miniaturized optical fiber formats.[7,8] These attributes render LSPR-based optical fiber sensors highly effective for label-free, real-time, and miniaturized detection in environmental and biosensing contexts.

In LSPR-based fiber sensors, the selection of plasmonic nanomaterials is a critical factor in determining sensitivity, spectral tunability, and operational stability. Gold and silver (Ag) monometallic nanoparticles are traditional choices for LSPR applications. In contrast, bimetallic Au–Pt nanostructures enable the simultaneous engineering of optical (plasmonic) and chemical properties through controlled composition and structural design, such as alloy, core–shell, or dendritic architectures.[11,12] The incorporation of platinum (Pt) alters the dielectric properties of the nanoparticles, resulting in shifts in the plasmon peak or changes in the spectral line shape compared to pure gold, thereby facilitating spectral tuning for optimal fiber interrogation and sensitivity.[13] Beyond optical enhancements, Pt imparts catalytic (peroxidase-like) activity and increased chemical robustness, resulting in a higher density of active sites for analyte adsorption and enhanced stability against oxidation or aggregation in complex environments.[11,14] Hybrid Au–Pt nanostructures can leverage plasmon-mediated interfacial charge transfer and plasmonic antenna effects to enhance analyte activation or reporter reactions. This dual functionality enables both optical and catalytic/colorimetric readouts, increasing detection reliability and lowering detection limits.[15] Experimental evidence suggests that well-designed Au@Pt and Au–Pt alloy nanoparticles retain strong LSPR responses while exhibiting catalytic activity, making them well-suited for compact fiber-optic LSPR probes for trace pesticide detection.[16]

In this work, we report the design and fabrication of a novel LSPR optical fiber sensor for the sensitive detection of Thiram and Quinalphos. We detail the synthesis of four distinct bimetallic Au@Pt core–shell nanostructures (designated Au@Pt 1–4) by systematically varying the Pt precursor concentration. These nanoparticles were extensively characterized by UV-Vis, EDS, FE-SEM, and HR-TEM, revealing a controlled morphological evolution from thin, smooth Pt shells to thick, highly dendritic structures. After immobilizing the optimized nanostructures onto the core of a multimode optical fiber *via* APTES silanization, the sensor was integrated into a PDMS microfluidic channel for performance evaluation. The sensing performance was systematically evaluated, demonstrating that the sensor functionalized with Au@Pt 3, which possesses an optimized dendritic morphology, exhibits superior sensitivity for Quinalphos with an ultra-low limit of detection (LOD). This study highlights the critical relationship between bimetallic nanostructure morphology and LSPR sensing enhancement, offering a promising platform for trace pesticide monitoring.

Experimental section

Materials and reagents

Gold(III) chloride trihydrate ($HAuCl_4 \cdot 3H_2O$, 99.9%), silver nitrate ($AgNO_3$, 99.0%), hexadecyltrimethylammonium bromide (CTAB, ≥99%), sodium borohydride ($NaBH_4$, ≥98%), L-ascorbic acid (AA, 99%), quinalphos ($C_{12}H_{15}N_2O_3PS$), thiram ($((CH_3)_2NCSS_2CSN(CH_3)_2)$), 3-aminopropyl triethoxysilane (APTES, 99%) was acquired from Sigma-Aldrich Co., MO, USA. Sodium hydroxide (NaOH, 96%) was purchased by Guangdong Guanghua Sci-Tech Co., Ltd (China). Sulfuric acid (H_2SO_4, 95%), ethanol (EtOH, C_2H_5OH, 99.8%) was provided by Fisher Ltd (UK).

Synthesis of Au NPs

The Au NPs were prepared through a reduction method by two-step procedures:

Preparation of gold nano seeds: A vial contained CTAB (7.5 mL, 0.1 M), $HAuCl_4$ (100 μL, 24 mM) and 1.8 mL of DI water under magnetic stirring at room temperature was added with $NaBH_4$ solution (0.6 mL, 0.01 M). The solution slowly turns from yellow to brown in color, and there is a presence of good sprouting. The sprouts are used within 2–5 hours (Scheme 1 and 2).

Then 240 μL Au seed was injected into the erlenmeyer flask with CTAB (100 mL, 0.1 M), $HAuCl_4$ (2.04 mL, 0.024 M), H_2SO_4

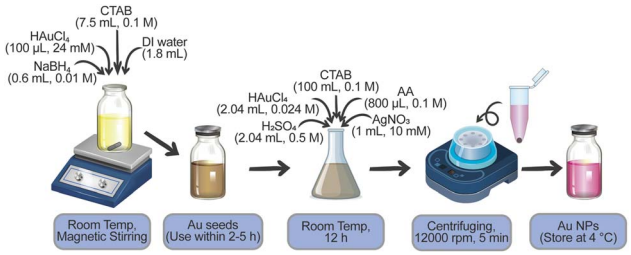

Scheme 1 Preparation process for Au NPs and Au@Pt NPs solutions.

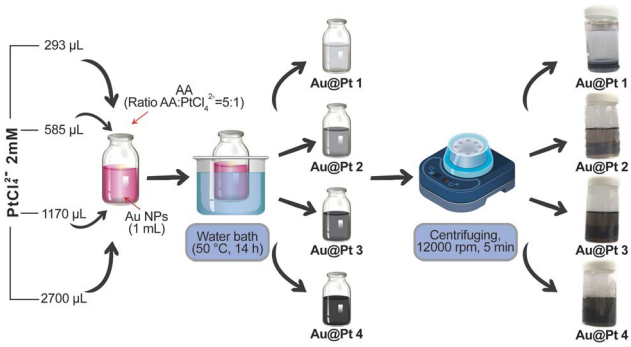

Scheme 2 Preparation process for Au@Pt NPs solutions.

(2.04 mL, 0.5 M), $AgNO_3$ (1 mL, 10 mM), and AA (800 µL, 0.1 M) for 12 h at room temperature, the solution turned light pink. The Au NPs were washed *via* centrifugation (12 000 rpm, 5 min), followed by redispersing them in DI water and kept in 4 °C. Throughout the material synthesis process, CTAB serves as an effective surface stabilizer, providing assistance in controlling AuNP formation and preventing aggregation. CTAB binds to AuNPs, forming micelle structures with positively charged (hydrophilic) tails pointing outwards. This creates electrostatic repulsion, preventing AuNPs from aggregating and allowing them to disperse effectively in aqueous environments. In addition, the rate of Au^{3+} reduction reaction is also slowed down due to the interaction of CTAB with the Au precursor, which helps to control and increase the uniformity of the AuNPs after formation.

Synthesis of Au@Pt NPs

Volumes of 2 mM $PtCl_4^{2-}$ (293, 585, 1170, 2700 µL) were added to the vial containing 1 mL of Au NPs, respectively. Then, a certain amount of AA was rapidly added to the vial with a ratio of AA : $PtCl_4^{2-}$ of 5 : 1. The solution was diluted to 3 mL, shaken vigorously, and kept in a well-conditioned bath for 14 h at 50 °C. The color of the solution slowly changed from pink to gray with intensity corresponding to the $PtCl_4^{2-}$ ratio. The final solution was centrifuged at 12 000 rpm for 5 min, then redispersed in 3 mL of DI water before being stored in the dark at 4 °C.

Fabrication of an integrated device of microfluidics and fiber-optic sensors

Multimode optical fibers were processed following the procedure reported in our previous work.[17] Briefly, 20 cm sections of multimode fiber were subjected to localized thermal treatment using a welding machine (ATC-2450-III, ARIM) at 350 °C to remove a 1 cm segment of the outer jacket at the center of the fiber. The exposed cladding layer was subsequently removed by immersing the treated region in a 3 : 2 (v/v) acetone: ethanol solution until the bare silica core was fully revealed.

Before surface silanization, the exposed silica region was activated by oxygen plasma treatment using a CUTE plasma system. The plasma activation step generated a high density of surface –OH groups, improving the uniformity and stability of the subsequent silane layer. Immediately after plasma activation, the fiber was immersed in an APTES solution in ethanol for 2 hours to form an aminosilane functional layer on the silica surface. The APTES-functionalized fiber segment was then immersed in the Au@Pt NPs suspension for 8 hours to immobilize the plasmonic nanostructures onto the activated surface.

Both ends of the fiber were stripped using a precision fiber stripping tool (Thorlabs; cladding/coating range: 385–430 µm/635–787 µm) and connected to fiber terminators (Thorlabs), enabling straightforward integration with the optical system *via* standard FC/PC multimode connectors.

In order to produce the microfluidic flow channel, PDMS was molded over a clean glass substrate to create straight-channel geometry with two access ports used as the inlet and outlet.[18] The PDMS prepolymer was made following the manufacturer's recommendations (Sylgard 184 kit, mixing elastomer base and curing agent in a 10 : 1 (v/v) proportion). After being well mixed, the solution was degassed under vacuum in a desiccator to eliminate entrapped air bubbles and attain homogeneous mold quality. Then the degassed mixture was poured into the channel mold and left at room temperature for natural curing overnight. Once fully crosslinked, the inlet and outlet holes were created using a 1 mm circular metal punch to enable fluid injection and flow through the microchannel.

Following the fabrication of the PDMS microfluidic layer, the functionalized optical fiber was carefully aligned along the straight channel region before sealing. The exposed sensing area of the fiber was positioned centrally within the channel to ensure uniform interaction with the flowing analyte solution. To immobilize the fiber and reinforce the mechanical stability of the microfluidic assembly, an additional amount of uncured PDMS was applied to both ends of the channel to encapsulate the fiber inlet and outlet regions. This PDMS coating served to firmly fix the fiber in place while simultaneously providing leak-free sealing around the fiber-PDMS interface. The entire structure was then left at room temperature to cure completely for subsequent sensing measurements.

Optical setups for optical biosensing technologies and measurements

The optical sensing experiments were performed using a 5 mW He–Ne laser source (LASOS LGK 7628) operating at 632.8 nm as the excitation wavelength. To ensure that only the guided light propagating through the fiber core was detected, stray light from the cladding was removed using an aperture-based collimator positioned in front of the detector. The transmitted

optical power was monitored with a handheld digital optical power meter (PM100D, Thorlabs, Newton, NJ, USA), which was interfaced with a computer for real-time acquisition and recording of the fiber sensor's output intensity (Scheme 3).

For fluid delivery, the optical fiber probe was integrated into a PDMS microfluidic chip, which was connected to a peristaltic pump (Eleya SMP-21, Japan) using flexible plastic tubing (inner/outer diameter: 1.15/3.2 mm). The pump provided controlled flow through the sensing region, with the flow rate set to complete each fluid exchange in approximately 1 minute, ensuring stable, repeatable analyte introduction during measurements. In this experiment, the output optical intensity was recorded continuously for 60 seconds, starting 5 minutes after the analyte solution was pumped into the channel, yielding 60 data points per measurement. This process was repeated 3 times at each analyte concentration.

Results and discussion

To explore the effect of Pt amount on the structural and optical properties of bimetallic NPs, four groups of Au@Pt NPs were synthesized by adjusting the volume of 2 mM $PtCl_4^{2-}$ precursor added to the growth solution. The samples were named as Au@Pt 1, Au@Pt 2, Au@Pt 3, and Au@Pt 4, corresponding to Pt precursor volumes of 293 μL, 585 μL, 1170 μL, and 2700 μL, respectively. This systematic variation in $PtCl_4^{2-}$ loading offers a means of precisely controlling the modification of the thickness of the Pt shell on the Au core, resulting in significant differences in morphology, surface coverage, and LSPR phenomena. These four nanoparticle sets, therefore, provide a basis for evaluating the Pt component's effect on the plasmonic response and sensing performance of the Au@Pt-functionalized optical fiber probes.

The UV-vis spectra of the Au NPs and Au@Pt NPs solutions are displayed in Fig. 1. The UV-vis absorption spectra of the prepared nanoparticles can provide clear evidence for the evolution of the structure conformation for Au@Pt nanostructures with different volumes of Pt precursor added. The pristine Au NPs display a sharp LSPR band at 540 nm ascribed to the spherical shape of Au NPs.[19] In contrast, all Au@Pt samples exhibit highly broadened plasmon peaks with resonance positions from approximately 515 to 631 nm depending on the volume of Pt. This feature is consistent with the commonly observed quenching of Au plasmons upon Pt deposition, where Pt causes a stronger interband absorption and introduces additional non-radiative decay channels, resulting in decreased LSPR intensity and peak broadening.[13,20] The experimentally observed spectral shifts reflect changes in the

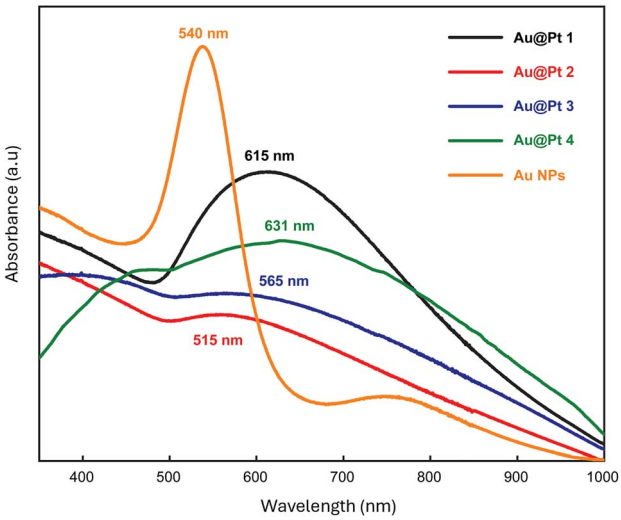

Fig. 1 UV-vis absorption spectra of the pristine Au NPs and Au@Pt NPs (samples 1–4).

effective dielectric environment and particle morphology of the bimetallic particles; as the Pt overlayer is added, there is a modification of the optical response through plasmon-metal coupling, different particle size, and possibly the formation of Pt islands or partial shells, which may affect hybridization between modes within Au core.[15,21] The increasing trend of the color change in the nanoparticle solutions, such as from pink (Au NPs) to greyish and dark-grey appearance (with high Pt content for Au@Pt), also implies more deposition of Pt because highly loaded Pt-based surfaces are able to broadly absorb across the visible width.[22] Such different spectral fingerprints also indicate the four Au@Pt samples have different Pt loadings and surface morphologies, and these can directly influence LSPR properties and sensing performance.

The EDS spectra of the four Au@Pt samples (Fig. 2) also confirm that both Au and Pt are contained in each. Typical Au lines are present in the low-energy (2 keV) as well as high-energy (9–12 keV) part of the spectrum. Pt signals are observed at

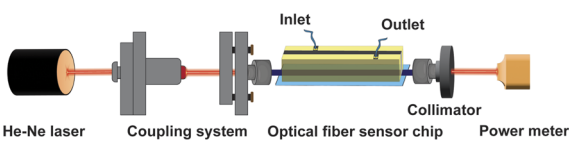

Scheme 3 Illustration of the system for measuring signals using a fiber optic sensor.

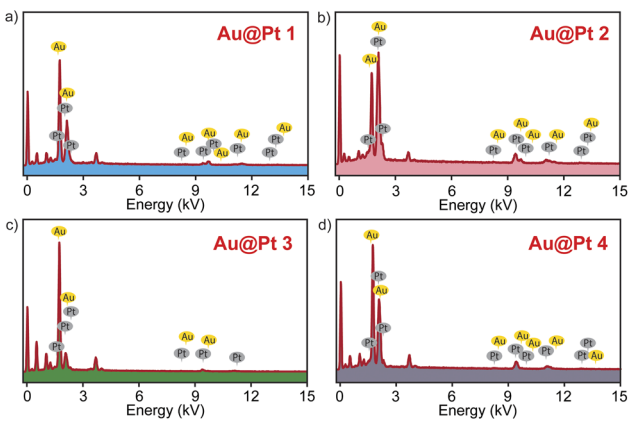

Fig. 2 EDS spectra of the synthesized Au@Pt NPs: (a) Au@Pt 1, (b) Au@Pt 2, (c) Au@Pt 3, and (d) Au@Pt 4.

expected energies (about 2 keV and between 9 and 11 keV) which partially overlap with the Au peaks although they can still be identified. The intensity of the Pt peaks increases with greater Pt precursor volumes, directly indicating higher Pt content in the respective samples. These EDS results confirm the successful deposition of Pt onto the Au nanoparticles in all samples.[23] These EDS features are characteristic of Au–Pt bimetallic nanostructures, where partial overlap of Au and Pt lines occurs due to their similar atomic numbers and X-ray energies.[21] Overall, the EDS results demonstrate that all synthesized samples contain both Au and Pt, with peak patterns consistent with those reported in the literature for core–shell or surface-decorated Au–Pt nanoparticles.[24]

Fig. 3 shows FE-SEM images of four Au@Pt NPs samples with different Pt precursors, which can show very obvious morphological differences along with Pt precursor increase. The Au@Pt 1 has the smaller and highly packed nanoparticles, with an average size of 43 ± 3 nm, aggregating delicate clusters (Fig. 3a). The surface texture is less defined, suggesting a more limited Pt deposition than in samples synthesized with a higher Pt precursor. In Au@Pt 2 (Fig. 3b), the nanoparticles are bigger and less alloyed with an average size of 63 ± 8 nm. Higher resolution of individual nanoparticles can be observed, which suggest that Pt growth is enhanced and particle size relative to Au@Pt 1 is also increased accordingly. The Au@Pt 3 sample (Fig. 3c) includes discrete, densely distributed spherical particles with an average size of 74 ± 9 nm. As compared to the samples prepared with lower or higher Pt precursor volumes, Au@Pt 3 presents better size uniformity and sharper particle edges, which suggests that the reaction volume of intermediate Pt precursor leads to increased Pt coverage. Au@Pt 4 (Fig. 3d) features the biggest particles of an average size of 106 ± 13 nm. These particles seem more aggregated, to form clusters with rougher surfaces probably because of the highest Pt loading. The gradual growth of particle size from Au@Pt 1 to Au@Pt 4 can be related to the increased Pt content in their synthesis and is consistent with those expected for Pt overgrowth on noble-metal nanocores.

HR-TEM images and HAADF-STEM elemental mapping were used to elucidate detailed morphology and elemental distribution (Fig. 4). The images confirm that all samples have a distinct core–shell architecture, with elemental maps showing a high-density Au core (yellow) encapsulated by a Pt shell (red). With exorbitant Pt precursor concentration, the Pt shell thickness and morphology change step by step: Au@Pt 1 (Fig. 4a) has a thin, smooth shell, and at just 3.5 ± 0.3 nm, it is the highest quality of any of these particles; Au@Pt 2 (Fig. 4b) has a thicker shell (6 ± 2 nm); Au@Pt 3 (Fig. 4c) exhibits a much thicker layered electric field (12.5 ± 1.5 nm) with dendritic texture on top of that; and the shell of Au@Pt 4 (Fig. 4d) is the thickest (29.4 ± 4.3 nm) and has the most highly developed dendritic fibrous structure. This systematic shell thickening, confirmed by HR-TEM, accounts for the overall increase in particle size observed in FE-SEM analysis (Fig. 3). TEM images (Fig. 4c and d) also clarify that the surface "roughness" seen in FE-SEM on larger particles corresponds to this dendritic structure. This progression matches EDS results (Fig. 2), where increased Pt shell thickness and volume correspond to a higher Pt elemental signal, confirming the direct relationship between precursor concentration, shell volume, and elemental composition.[25] FESEM and HRTEM images at different magnifications of the Au@Pt samples (1, 2, 3, and 4) presented in Fig. S1 and S2 provide an overview and evidence of the morphology, uniformity, and structure of the Au@Pt samples.

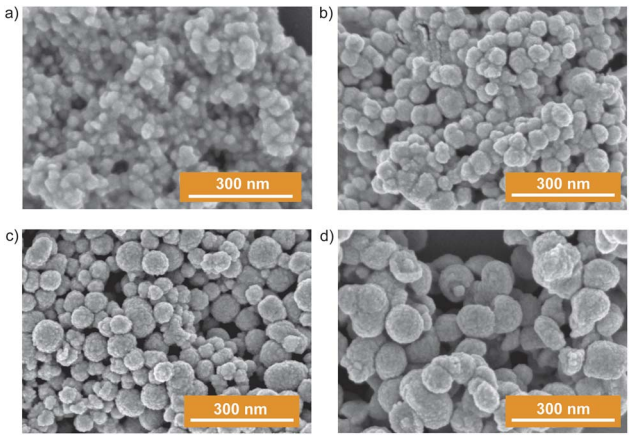

Fig. 3 FE-SEM micrographs of the Au@Pt NPs: (a) Au@Pt 1, (b) Au@Pt 2, (c) Au@Pt 3, and (d) Au@Pt 4.

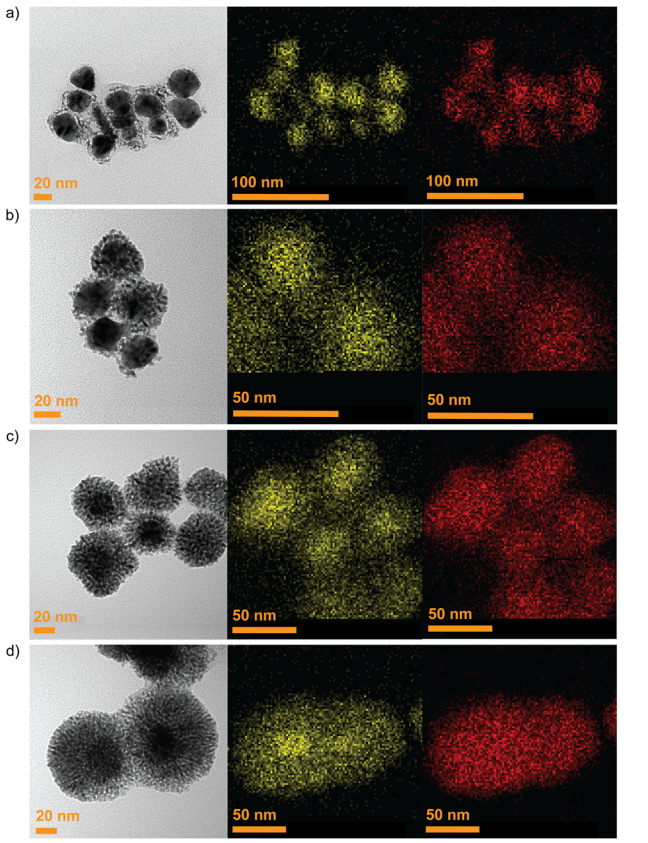

Fig. 4 HR-TEM images and HAADF-STEM elemental mapping of: (a) Au@Pt 1, (b) Au@Pt 2, (c) Au@Pt 3, and (d) Au@Pt 4.

The sensing properties of four different Au@Pt NPs functionalized optical fiber probes were evaluated by monitoring the response in the output power to various concentrations of Quinalphos (Fig. 5a–d). For all sensor designs the dose-dependent behavior could clearly be seen, comprised of a rapid rise in output power for low concentrations and a slow approach to saturation. This indicates that there is very strong interaction and high affinity between the sensor surface and Quinalphos analyte. To enable quantitative comparison, the LOD was determined for each sensor. The calibration curves constructed according to the Belehradek mode, shown in Fig. 5, demonstrate the trend of light transmission intensity as a function of Quinalphos concentration. The sensor sensitivity is calculated using the data-fitting equation from the Belehradek mode. Based on the power sensitivity value at a give Quinalphos concentration, the detection limit is determined by the formula: LOD $= 3\sigma/S$ (where, σ is the standard deviation of the blank signal, and S is the sensor's sensitivity). Sensors functionalized with Au@Pt 1 (Fig. 5a) and Au@Pt 2 (Fig. 5b) demonstrated high sensitivity, with LODs of 1.78×10^{-13} M and 8.85×10^{-14} M, corresponding to correlation coefficients R^2 of 0.9365 and 0.9608, respectively. By comparison, the Au@Pt 4 sensor (Fig. 5d) exhibited the lowest sensitivity, with an LOD of 7.09×10^{-14} M, and an R^2 of 0.9886. Surprisingly, the Au@Pt 3 sensor (Fig. 5c) gave an ultralow LOD of 1.73×10^{-14} M corresponding to $R^2 = 0.9438$. This improvement in sensitivity is attributed to the special morphology of the Au@Pt 3 nanoparticle magnet as observed by HR-TEM (Fig. 4c). Unlike the smoother, thinner shells of samples 1 and 2, the Au@Pt 3 sample features a well-developed dendritic structure with a 12.5 nm shell thickness. This morphology offers significant advantages for LSPR sensing by providing a substantially increased effective surface area, thereby enriching the number of available binding sites for Quinalphos molecules.[26] Additionally, the numerous sharp tips act as plasmonic "hot spots" that concentrate the local electromagnetic field, thereby amplifying the optical response even when only a few molecules bind to these sites.[27] The reduced performance of Au@Pt 4,

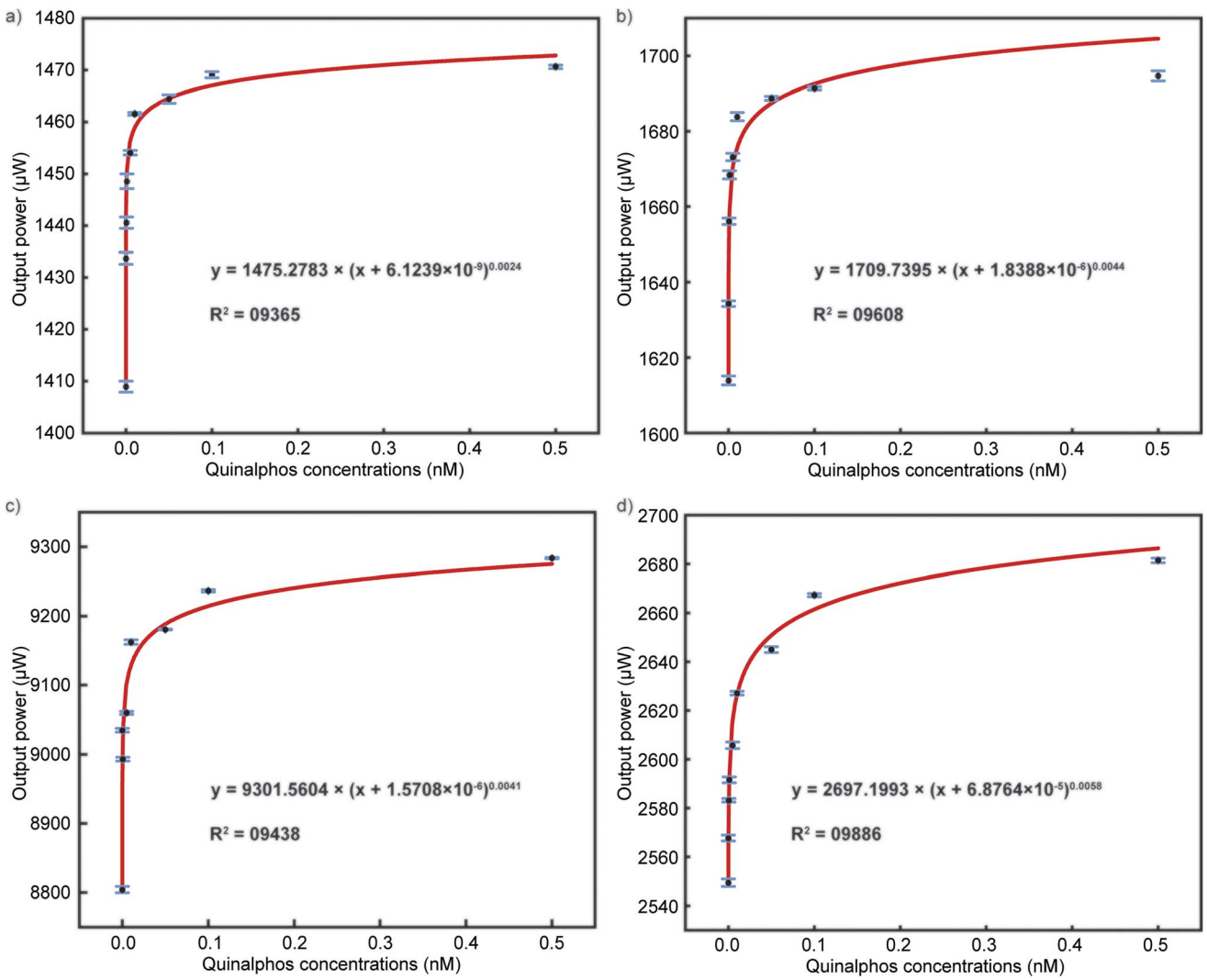

Fig. 5 Output power response of optical fiber probes functionalized with different Au@Pt NPs: (a) Au@Pt 1, (b) Au@Pt 2, (c) Au@Pt 3, and (d) Au@Pt 4 upon exposure to increasing concentrations of Quinalphos.

despite its dendritic structure, is likely due to its significantly thicker Pt shell (29.4 nm), which causes excessive plasmon damping of the Au core's resonance.[28] This damping effect, observed in the UV-vis spectra, likely reduces the sensor's responsiveness to surface binding events. Table 1 presents LOD statistics from recent Quinalphos detection studies, highlighting the superior performance of fiber-optic LSPR sensors compared to other methods. Overall, the Au@Pt 3 nanostructure achieves an optimal balance between high surface area and substantial, accessible plasmonic field enhancement, resulting in the observed ultra-low detection limit. Furthermore, the synergistic effect of combining the two metals Au and Pt enhances dielectric sensitivity by many times compared to conventional Au particles. Feng *et al.* demonstrated computationally that the LSPR wavelength shift in Au@Pt, due to the refractive index, is increased by more than 22% compared to AuNPs.[29] Structurally, the Quinalphos molecule contains an =S group, which has a strong affinity for AuNPs, enabling Quinalphos to adsorb readily onto the surface of Au@Pt materials. At this point, the Pt nano-branches come into contact with the analyte molecules, leading to a change in surface charge that causes a red shift in the LSPR peak of Au@Pt. Simultaneously, Quinalphos is adsorbed onto the Au@Pt surface, forming a coating that reduces the material's absorption intensity. This is consistent with the increase in output power with Quinalphos concentration recorded for all four Au@Pt samples.

After optimization with Quinalphos, the Au@Pt 3 sensor was further evaluated for the detection of Thiram, a dithiocarbamate fungicide, to demonstrate its versatile sensing capabilities. Dynamic response of the sensor as a function of the LOD is shown to analyze performance between 10^{-3} and 10^{-11} M concentration (Fig. 6a) where different power levels are observed for respective concentration values. Calibration curves (Fig. 6b) demonstrated a good linear relationship ($R^2 = 0.987$) between output power and the negative logarithm of Thiram concentration ($-\mathrm{Log}\ C$). The linear regression equation, $y = 2.00 \times 10^{-6}x + 3.95 \times 10^{-4}$, validated the quantitative reliability in a broad dynamic range. The LOD obtained was 1.37×10^{-11} M, which is quite competitive for trace pesticide analysis. This performance is ascribed to the high specific surface area and numerous plasmonic "hot spots" of the dendritic Au@Pt 3 nanostructure, which can promote the process of analyte absorption and then signal amplification.[30] Similar to Quinalphos, Thiram also contains =S functional groups that have a strong affinity for AuNPs, thus readily adsorbing onto the surface of Au@Pt materials, causing a shift in the LSPR peak and a sharp decrease in the material's adsorption capacity. This is the main reason the output optical transmission power increases proportionally with Thiram concentration. In order to test robustness, the reproducibility of the measurements (Fig. 6c) was evaluated and an relative standard deviation (RSD) of 1.67% was obtained from 11 separate measurements, demonstrating a good repeatability of signals. Stability measurement in the short term was conducted at 5 min (300 s) intervals as shown in Fig. 6d, and a stable response with a coefficient of variation (CV) of < 0.1% can be observed for the sensor. Collectively, these results demonstrate that the Au@Pt 3 probe is a stable, reproducible, and highly sensitive platform for detecting a wide range of pesticide residues.

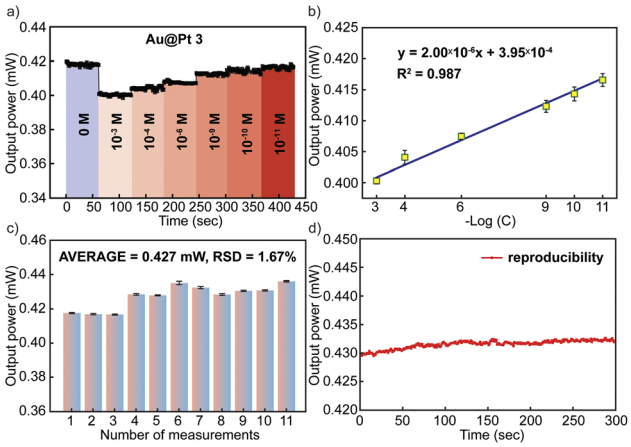

Fig. 6 Evaluation of the optimized Au@Pt 3 sensor for Thiram detection: (a) real-time dynamic response to varying Thiram concentrations (10^{-3} M to 10^{-11} M); (b) standard curve of output power *versus* the negative logarithm of concentration; (c) reproducibility test across 11 independent measurements; and (d) short-term stability analysis over 300 seconds.

To underscore the superior performance of the fabricated sensors, particularly the Au@Pt 3 design, it is noteworthy to compare these findings with state-of-the-art optical fiber sensors recently developed for pesticide detection. For instance, Moslemi *et al.* (2024) fabricated an LSPR-sensing fiber-optic probe in reflective mode for the detection of Thiram, functionalized with a gold nanoparticle *via* layer-by-layer assembly, with a LOD of 6×10^{-8} M.[31] With the advantage of a compact probe suitable for confined environments, and high accuracy

Table 1 A comparison between the recently reported and the sensor based on Au@Pt NPs in detecting Quinalphos

Material	Method	LOD (M)	Ref.
2-Amino-4-thiazoleacetic acid anchored AuNPs	Spectrophotometric probe	48×10^{-9}	33
Polyvinyl alcohol/gelatin-gold nanoparticles nanofiber membrane	Electrochemical	17×10^{-11}	34
Cu(II)–Au@ONP	Fluorescence	2.4×10^{-9}	35
Grewia asiatica-carbon dots	Fluorescence	1.46×10^{-9}	36
OPCD@UiO-66-NH_2	Fluorescence	3×10^{-10}	37
Trypsin encapsulated Au–Ag nanoclusters	Fluorescence	3.2×10^{-8}	38
Au@Pt	LSPR optical fiber	1.73×10^{-14}	This study

due to less influence from the surrounding environment compared to transmissive mode LSPR sensors. However, sensitivity is often lower due to the limited sensing area. In another study by Akavaram *et al.* (2021), trypsin-encapsulated Au–Ag bimetallic nanoclusters are used to demonstrate fluorescence-quenching-based detection of Quinalphos with a LOD of 32×10^{-8} M.[32] Their bimetallic approach improved stability under environmental conditions and reduced signal overlap from sample components; however, sensitivity remains limited to the micromolar range. In stark contrast, our Au@Pt 3 dendritic sensor achieved an ultralow LOD of 1.73×10^{-14} M for Quinalphos and 1.37×10^{-11} M for Thiram. This dramatic enhancement highlights the critical role of the dendritic morphology and the specific synergistic effect of the Au core and Pt shell in amplifying the LSPR signal, far exceeding the performance of conventional bimetallic nanoclusters.

Conclusions

In conclusion, a simple and highly sensitive LSPR optical fiber sensor has been successfully fabricated using bimetallic Au@Pt core–shell NPs for trace detection of organophosphorus and dithiocarbamate pesticides. Using a controllable seed-mediated growth strategy, we have shown that the Pt shell morphology can be systematically managed by tuning the precursor concentration. Structural characterization confirmed a transition from thin, smooth shells to thick, dendritic structures, with the Au@Pt 3 sample exhibiting a unique urchin-like morphology that maximizes plasmonic field enhancements. The sensing studies showed that this dendritic shape is of key importance for applications, as the Au@Pt 3 probe outperforms other material configurations. The sensor showed good sensitivity with LODs of 1.73×10^{-14} M for Quinalphos and 1.37×10^{-11} M for Thiram. Furthermore, the device also exhibited good reproducibility, stability and a broad linear-response range. This work not only highlights the significance of morphological design on bimetallic nanostructures but also offers a potential development combining a low-cost, effective and practical platform for the determination of hazardous pesticide residues in agricultural and environmental samples in real time.

Author contributions

Nguyen Tran Truc Phuong: synthesis, formal analysis, investigation, writing – original draft; Nguyen Do Quynh Nhu: formal analysis, writing – original draft; Le Hong Tho: data curation, measurement; Do Thao Anh: analysis, interpretation; Quan-Doan Mai: investigation, interpretation; Vu Thi Huong: synthesis, formal analysis; Ting Yu-Liu: measurement, analysis; Khanh Q.Kieu: methodology, formal analysis; Duc Anh Dinh: interpretation, measurement; Nhu Hoa Thi Tran: conceptualization, investigation, writing – review & editing, supervision.

Conflicts of interest

There are no conflicts to declare.

Data availability

The data supporting this article have been included as part of the supplementary information (SI). Supplementary information is available. See DOI: https://doi.org/10.1039/d6ra01129b.

Acknowledgements

We acknowledge Nguyen Tat Thanh University, Ho Chi Minh city, Vietnam for supporting this study. This study was supported by Vietnam National University, Ho Chi Minh City (grant no. TX2026-82-01).

Notes and references

1 M. Anastassiadou, G. Bernasconi, A. Brancato, L. Carrasco Cabrera, L. Ferreira, L. Greco, S. Jarrah, A. Kazocina, R. Leuschner, J. O. Magrans, I. Miron, S. Nave, R. Pedersen, H. Reich, A. Rojas, A. Sacchi, M. Santos, A. P. Scarlato, A. Theobald, B. Vagenende and A. Verani, *EFSA J.*, 2021, **19**, e06391.
2 A. Jamal, M. I. Ali, A. Bin Masood, M. K. Wazir, A. Ullah and R. Rehman, in *Industrial Applications of Biosurfactants and Microorganisms: Green Technology Avenues from Lab to Commercialization*, Academic Press, 2023, pp. 121–149.
3 C. Jansson, T. Pihlström, B. G. Österdahl and K. E. Markides, *J. Chromatogr. A*, 2004, **1023**, 93–104.
4 S. T. Narenderan, S. N. Meyyanathan and B. Babu, *Food Res. Int.*, 2020, **133**, 109141.
5 P. R. Boro, P. P. Borthakur and E. Baruah, in *Engineering Proceedings 2025*, Multidisciplinary Digital Publishing Institute, 2025, vol. 106, p. 6.
6 N. I. M. Fauzi, Y. W. Fen, N. A. S. Omar and H. S. Hashim, *Sensors*, 2021, **21**, 3856.
7 I. Del Villar and I. R. Matias, *Optical Fibre Sensors: Fundamentals for Development of Optimized Devices*, Wiley, 2020.
8 J. Castrellon-Uribe, in *Fiber Optic Sensors*, IntechOpen, 2012.
9 C. Pendão and I. Silva, *Sensors*, 2022, **22**, 7554.
10 Z. Fang, K. K. Chin, R. Qu and H. Cai, *Fundamentals of Optical Fiber Sensors*, John Wiley and Sons, 2012.
11 M. Zhang and X. Guo, *Coord. Chem. Rev.*, 2022, **465**, 214578.
12 S. He, Z. Tang, T. Huo, D. Wu and J. H. Tang, *J. Manuf. Mater. Process.*, 2025, **9**, 131.
13 C. Langhammer, Z. Yuan, I. Zorić and B. Kasemo, *Nano Lett.*, 2006, **6**, 833–838.
14 Y. Wang and Y. Xianyu, *Biosens. Bioelectron.*, 2023, **237**, 115553.
15 D. C. Ratchford, *ACS Nano*, 2019, **13**, 13610–13614.
16 Z. Fu, W. Zeng, S. Cai, H. Li, J. Ding, C. Wang, Y. Chen, N. Han and R. Yang, *J. Colloid Interface Sci.*, 2021, **604**, 113–121.
17 N. T. Truc Phuong, V. Q. Dang, L. Van Hieu, T. N. Bach, B. X. Khuyen, H. K. Thi Ta, H. Ju, B. T. Phan and N. H. Thi Tran, *RSC Adv.*, 2022, **12**, 31352–31362.
18 N. La Ngoc Tran, D. Van Hoang, A. Tuan Thanh Pham, N. Tran Truc Phuong, N. Xuan Dat Mai, T. T. K. Chi,

B. T. T. Hien, T. Bach Phan and N. H. T. Tran, *J. Sci. Adv. Mater. Devices*, 2023, **8**, 100584.
19 D. Liu, C. Li, F. Zhou, T. Zhang, H. Zhang, X. Li, G. Duan, W. Cai and Y. Li, *Sci. Rep.*, 2015, **5**, 7686.
20 E. Demishkevich, A. Zyubin, A. Seteikin, I. Samusev, I. Park, C. K. Hwangbo, E. H. Choi and G. J. Lee, *Materials*, 2023, **16**, 3342.
21 A. Higareda, S. Kumar-Krishnan, A. F. García-Ruiz, J. Maya-Cornejo, J. L. Lopez-Miranda, D. Bahena, G. Rosas, R. Pérez and R. Esparza, *Nanomaterials*, 2019, **9**, 1644.
22 R. Li, W. Chen, H. Kobayashi and C. Ma, *Green Chem.*, 2010, **12**, 212–221.
23 D. Garcia-Gutierrez, C. Gutierrez-Wing, M. Miki-Yoshida and M. Jose-Yacaman, *Appl. Phys. A Mater. Sci. Process.*, 2004, **79**, 481–487.
24 W. Hong and C. W. Li, *ACS Appl. Mater. Interfaces*, 2019, **11**, 30977–30986.
25 I. Maack, K. Oldenburg and K. Al-Shamery, *CrystEngComm*, 2024, **26**, 6748–6756.
26 M. Sanders, Y. Lin, J. Wei, T. Bono and R. G. Lindquist, *Biosens. Bioelectron.*, 2014, **61**, 95–101.
27 C. L. Nehl, H. Liao and J. H. Hafner, *Nano Lett.*, 2006, **6**, 683–688.
28 M. Elabbadi, C. Boukouvala and E. Ringe, *Sci. Rep.*, 2025, **15**, 1292.
29 L. Feng, X. Wu, L. Ren, Y. Xiang, W. He, K. Zhang, W. Zhou and S. Xie, *Chem. –Eur J.*, 2008, **14**, 9764–9771.
30 D. Wang and Y. Li, *Adv. Mater.*, 2011, **23**, 1044–1060.
31 A. Moslemi, L. Sansone, F. Esposito, S. Campopiano, M. Giordano and A. Iadicicco, *Opt. Laser Technol.*, 2024, **175**, 110882.
32 S. Akavaram, M. L. Desai, T. J. Park, Z. V. P. Murthy and S. K. Kailsa, *J. Mol. Liq.*, 2021, **327**, 114830.
33 C. Loganathan, N. S. K. Gowthaman and S. Abraham John, *Microchem. J.*, 2021, **168**, 106495.
34 J. cheng Hu, P. Wen, Y. Wang, J. yi Yang, Z. li Xiao, Z. lin Xu, Y. dong Shen, H. Wang and B. D. Hammock, *Food Control*, 2024, **162**, 110423.
35 R. Rani, Mayank, P. Thangarasu and N. Singh, *ACS Appl. Nano Mater.*, 2019, **2**, 1–5.
36 F. Y. Vadia, S. Jha, V. N. Mehta, T. J. Park, N. I. Malek and S. K. Kailasa, *J. Photochem. Photobiol., A*, 2025, **458**, 115948.
37 M. K. Bera, L. Behera and S. Mohapatra, *Colloids Surf., A*, 2021, **624**, 126792.
38 S. Akavaram, M. L. Desai, T. J. Park, Z. V. P. Murthy and S. K. Kailsa, *J. Mol. Liq.*, 2021, **327**, 114830.